Location of high-affinity metal binding sites in the profile structure of the Ca^{+2}-ATPase in the sarcoplasmic reticulum by resonance x-ray diffraction

Francisco J. Asturias and J. Kent Blasie
Department of Chemistry, University of Pennsylvania, Philadelphia, Pennsylvania 19104 USA

ABSTRACT Resonance x-ray diffraction measurements on the lamellar diffraction from oriented multilayers of isolated sarcoplasmic reticulum (SR) membranes containing a small concentration of lanthanide (III) ions (lanthanide/protein molar ratio ~4) have allowed us to calculate both the electron density profile of the SR membrane and the separate electron density profile of the resonant lanthanide atoms bound to the membrane to a relatively low spatial resolution of ~40 Å. Analysis of the membrane electron density profile and modeling of the separate low resolution lanthanide atom profile, using step-function electron density models based on the assumption that metal binding sites in the membrane profile are discrete and localized, resulted in the identification of a minimum of three such binding sites in the membrane profile. Two of these sites are low-affinity, low-occupancy sites identified with the two phospholipid polar headgroup regions of the lipid bilayer within the membrane profile. Up to 20% of the total lanthanide (III) ions bind to these low-affinity sites. The third site has relatively high affinity for lanthanide ion binding; its K_a is roughly an order of magnitude larger than that for the lower affinity polar headgroup sites. Approximately 80% of the total lanthanide ions present in the sample are bound to this high-affinity site, which is located in the "stalk" portion of the "headpiece" within the profile structure of the Ca^{+2} ATPase protein, approximately 12 Å outside of the phospholipid polar headgroups on the extravesicular side of the membrane profile. Based on the nature of our results and on previous reports in the literature concerning the ability of lanthanide (III) ions to function as Ca^{+2} analogues for the Ca^{+2} ATPase we suggest that we have located a high-affinity metal binding site in the membrane profile which is involved in the active transport of Ca^{+2} ions across the SR membrane by the Ca^{+2} ATPase.

INTRODUCTION

The Ca^{+2} ATPase of the sarcoplasmic reticulum (SR) is an enzyme that utilizes energy obtained from hydrolysis of ATP to actively transport Ca^{+2} across the SR membrane against a maximal concentration gradient of $\sim 10^3$ M (1). The Ca^{+2} ATPase adopts several distinct conformations during the Ca^{+2} transport cycle (2). In what can be considered the initial step of the Ca^{+2}-transport process, two Ca^{+2} ions bind with high affinity ($K_a \sim 10^6$ M, [3]) to what is known as the E_1 conformation of the enzyme. Besides their very high affinity, the Ca^{+2} binding sites in this enzyme conformation are also very selective. For example, binding of Ca^{+2} occurs in the presence of a Mg^{+2} concentration that is three orders of magnitude higher than the Ca^{+2} concentration (4). After phosphorylation of the enzyme by a metal · ATP substrate, formation of the $E_1 \sim P$ intermediate enzyme conformation and "occlusion" of the Ca^{+2} ions bound to the high-affinity binding sites take place (5). The Ca^{+2} ions bound to the Ca^{+2} ATPase are then translocated across the SR membrane and released in the lumen of the SR from low-affinity ($K_a \sim 10^3$ M) binding sites on the $E_2 \sim P$ conformation of the ATPase (3). Knowledge of the location of the Ca^{+2} ions in the membrane profile for each intermediate conformation of the Ca^{+2} ATPase occurring during the active transport process, would greatly contribute to a better understanding of the mechanism of action of this ATPase, and quite possibly other membrane proteins responsible for active ion transport. The obvious first step toward this goal is to localize the Ca^{+2} high-affinity binding sites in the SR membrane profile for the E_1 conformation (resting state) of the Ca^{+2} ATPase protein. It was previously proposed on the basis of the amino-acid sequence and the predicted secondary/tertiary structure of the protein (6, 7) that the Ca^{+2} high-affinity binding sites were probably located in the "stalk" portion of the ATPase "headpiece," i.e., in that section of the profile structure of the protein connecting the portion within the lipid bilayer with the large mass of protein located outside the membrane lipid bilayer and protruding into the extravesicular space (8). However, recent studies involving site-specific mutagenesis of individual residues in the Ca^{+2} ATPase enzyme, and their effect on Ca^{+2} transport and enzyme activation (9, 10), suggest that residues in the "stalk" region of the protein are involved in Ca^{+2} transport, but that the residues that form the high affinity Ca^{+2} binding site involved in activation of the enzyme are probably located in the transmembranous region the putative model of the Ca^{+2} ATPase structure.

The technique of resonance (or anomalous) x-ray

0006-3495/91/02/488/15 $2.00

diffraction can be used to determine with high precision the position of particular atoms within large noncrystalline structures such as biological membranes (11, 12). The technique is based on the large changes in the x-ray scattering amplitude of an atom at energies near an atom's absorption edge (13). Resonance x-ray diffraction can locate a particular atom in a way that is analogous to that of isomorphous replacement (14), but the resonance technique has the obvious advantage that no modification of the system is necessary. The availability of synchrotrons as high flux, tunable x-ray sources has made such resonance x-ray diffraction experiments feasible. Furthermore, time-resolved resonance x-ray diffraction could in principle be used to follow the location of the Ca^{+2} ions in the SR membrane profile during active transport, allowing a direct "visualization" of the calcium occlusion ($E_1 \Rightarrow E_1 \sim P$) and traslocation ($E_1 \sim P \Rightarrow E_2 \sim P$) steps.

The use of resonance x-ray diffraction to determine the position of the Ca^{+2} high-affinity binding sites in the SR membrane profile presents some technical difficulty due to the relatively low x-ray energy of the calcium K absorption edge (4.04 keV), that results in strong absorption effects in the oriented multilayer sample. This can be overcome by the use of lanthanide (III) ions as Ca^{+2} "analogues" because their L absorption edges occur at substantially higher x-ray energies. Lanthanide (III) ions have been extensively used as substitutes for divalent ions such as Ca^{+2} in biological systems (15). Numerous reports in the literature indicate that lanthanide (III) ions compete with Ca^{+2} ions for high-affinity binding sites in the Ca^{+2} ATPase (16–19). The use of lanthanide ions as Ca^{+2} analogues for resonance x-ray diffraction experiments has the additional advantage that the resonance effects at the lanthanide L_{III} absorption edge used for the resonance experiment are significantly larger than the effects that would be observed at the Ca K edge (6–7 electrons vs. ~20 electrons), a fact that facilitates the location of the two metal atoms bound to a protein of molecular weight ~110,000 (6, 20), in a membrane with a phospholipid/protein ratio of ~110 (8).

This paper describes the results of the necessary first step in the use of time-resolved resonance x-ray diffraction to follow the location of Ca^{+2} ions in the SR membrane profile during the active transport process. Resonance x-ray scattering effects about the La and Tb L_{III} absorption edges on the lamellar diffraction from oriented multilayers of SR membrane vesicles for lanthanide/protein mole ratios of ~4 were directly analyzed to determine the location of the high- and low-affinity metal binding sites in the SR membrane profile for the E_1 (resting) conformation of the Ca^{+2} ATPase protein.

METHODS

Preparation of SR vesicular dispersions and oriented SR multilayers

Dispersions of SR membrane vesicles were prepared from albino rabbit hind leg muscle (21). The SR preparation was further purified by sucrose density gradient centrifugation as described previously (22). The purified SR preparation (at least 90% of the protein present was Ca^{+2} ATPase [22]) was stored at −70°C, suspended in a buffer containing 100 mM KCl, 2mM Tris maleate, at pH 6.85. Typical protein concentrations in these vesicular dispersions (determined by the Lowry method [23]) were ~10 mg protein/mL. Purified SR vesicular dispersions prepared as described above contain significant concentrations of both Ca^{+2} and Mg^{+2} ($[Ca^{+2}] \leq 20$ μM, $[Mg^{+2}] < 10$ μM; measured spectrophotometrically using the metallochromic indicator Arsenazo III). To ensure that the presence of Ca^{+2} and/or Mg^{+2} would not interfere with binding of the lanthanide (III) ions to the Ca^{+2} ATPase, the divalent metal ion content in the SR dispersions was reduced by treating them with EGTA (ethylene glycol-bis[β-aminoethyl ether] *N,N,N',N'*-tetraacetic acid; Sigma Chemical Co., St. Louis, MO), and subsequently washing them with a divalent metal free buffer (treated with Chelex-100; Bio-Rad Laboratories, Richmond CA) via dilution and centrifugation. The final SR dispersion from which the multilayer samples were prepared contained ~6 μM Ca^{+2} ATPase protein, ~1 μM free divalent metal ions, and ~1 μM EGTA. To prepare oriented multilayer samples, an appropriate volume of this "divalent-metal-free" SR dispersion (~2 mL, containing 1.2 mg of protein) was placed in a sedimentation cell and an appropriate volume of a freshly prepared $LaCl_3$ or $TbCl_3$ solution was added (enough to obtain the desired lanthanide/protein mole ratio of ~4). The dispersion was then centrifuged (10^4 g, 45 min) to sediment the SR vesicles on to a flat aluminum foil substrate, and the resulting "pellet" was partially dehydrated under controlled relative humidity conditions (88% relative humidity) to form an oriented SR membrane multilayer sample as described previously (24).

Resonance diffraction data collection

Lamellar x-ray diffraction data from oriented, partially dehydrated SR multilayers was collected as a function of the reciprocal space coordinate z^*, ($z^* = 2 \sin\theta/\lambda$). Diffraction along this z^* axis corresponds to elastic photon momentum transfer parallel to the real space axis z, defined as perpendicular to the plane (on average) of the membranes of the flattened vesicles in the multilayer sample. Diffracted intensity along z^* arises from the so-called multilayer electron density profile, i.e., the projection onto the z-axis of the multilayer electron density along planes perpendicular to the z-axis (25).

The x-ray diffraction data was collected utilizing the Biostructures Participating Research Team beamline X-9A at the National Synchrotron Light Source, Brookhaven National Laboratory (Upton, NY). During data collection the synchrotron operated at an electron energy of 2.5 GeV, and the current in the ring decayed during a fill from 200 to 90 mA. A constant-exit-height, double Si (111) crystal monochromator was used to select the energy of the x-ray radiation incident on the samples. Radiation from the monochromator (FWHM 2.5 eV) was collected and linearly focused using a cylindrically bent horizontal mirror (Ni-coated Al) with its center at 1340 cm from the bending-magnet source. Cylindrically curved multilayer samples were mounted on a 4-circle diffractometer (Huber, FRG), with their surface centered on, and parallel to the ω-axis. A low-impedance, one-dimensional position sensitive detector mounted on the 2θ axis 680 mm from the

ω-axis was used to record the diffracted intensity along z^* in the 2θ plane. The linear position sensitive detector was interfaced to a multichanel analyzer and the full active length of the detector (100 mm) was digitized into 1,024 channels. A PDP 11/23 computer (Digital Equipment Corp., Marlboro, MA) was used to control the diffractometer and the electronics associated with the detector. The linearly focused x-ray beam had a FWHM of 0.25 mm at the detector in the z^*-direction. A N_2-filled ionization chamber was used to monitor the incident beam intensity I_0. The cylindrically curved multilayer samples were mounted in sealed cannisters with Mylar windows, and the relative humidity inside the cannisters was regulated using a saturated KCl solution (~88% relative humidity at 5°C). The temperature of the samples was maintained at 7 ± 1°C during partial dehydration and data collection (namely, above the characteristic temperature for lateral lipid phase separation for these SR membranes under these conditions [26]). For each sample, resonance lamellar diffraction data was collected for seven different energies: the energy corresponding to the L_{III} absorption edge of the particular lanthanide (La or Tb) in the sample, and the edge energy ±200 eV, ±100 eV, and ±50 eV. Data at the different energies was collected cyclically, such that an edge-energy measurement always preceded and followed data collected at two energies symmetrically displaced about the absorption edge. For selected samples, an additional set of "resonance" diffraction data about the L_{III} absorption edge of the alternate lanthanide (not present in the sample) was recorded as a control. Diffraction data were collected at fixed ω angle (because the multilayer samples were already cylindrically curved about ω) for 1,800 s at each energy. The patterns so recorded generally extended to a z^*_{max} corresponding to a limited spatial resolution of ~40 Å in the multilayer profile.

Diffraction data reduction

The detector channel corresponding to the z^*-origin was determined as that centered in the approximately symmetric diffraction evident in the raw lamellar intensity patterns recorded as total x-ray counts per channel along the active length of the detector for each x-ray energy E. The detector channel coordinate was then converted to the reciprocal space coordinate $z^* = 2 \sin \theta/\lambda$ using the appropriate constants determined during the positional linearity calibration of the detector. For patterns corresponding to off-edge energies, the intensity vs. z^* data were interpolated at equal intervals of z^* to match those z^*-values in the corresponding edge energy scans. The resulting lamellar diffraction patterns were then normalized to compensate for nonresonance differences in total integrated (over z^*) intensity, which also resulted in identical lamellar background scattering from the multilayers independently of x-ray energy. The normalized diffraction patterns were than corrected to account for the estimated lamellar background scattering by sustracting precisely the same[1] piece-wise continuous exponential function chosen to zero a majority of the intensity minima in the raw lamellar intensity functions $I_t(z^*, E)$. A Lorentz correction (8, 24) proportional to $(z^*)^2$ was then applied to the background-corrected patterns $I_c(z^*, E)$ to account for the cylindrical curvature and mosaic spread (inherent layer misorientation) of the multilayer samples. The stability of the multilayer samples as a function of time, as well as differences in the lamellar intensity functions presumably due to resonance effects, were judged by examining the arithmetic differences between appropriate diffraction patterns, $\Delta I_t(z^*, E_{ij} \equiv [I_t(z^*, E_i) - I_t(z^*, E_j)]$ both as a continuous function of z^*, and over successive constant integration intervals Δz^*. Only off-edge energy patterns included between subsequent edge-energy patterns for which essentially no time-dependent changes could be observed were used for further analysis.

[1]In order to *rigorously* apply this criterion, the estimated lamellar background scattering was subtracted only from the well off-resonance $I_t(z^*, \text{edge} + 200 \text{ eV})$ data, to provide $I_c(z^*, \text{edge} + 200 \text{ eV})$. The remaining $I_c(z^*, E)$ data were then calculated as:

$$I_c(z^*, E) = I_c(z^*, \text{edge} + 200\,ev) - [I_t(z^*, \text{edge} + 200\,ev) - I_t(z^*, E)].$$

Resonance diffraction effects

The energy-dependent scattering factor for the jth atom in a structure can be written (27):

$$f_j = f_j^\circ + f'_j(E) + if''_j(E) = f_j^t(E) + if_j^i(E), \quad (1)$$

where $f_j^t(E)$ and $f_j^i(E)$ represent the real and imaginary components of the atomic scattering factor, and the energy dependence of f_j is significant only if the jth atom in the structure has an absorption edge at a x-ray energy near that used to record the x-ray diffraction from the structure. The structure factor as a function of z^* for a multilayer composed of N atoms, which is the Fourier transform of the multilayer electron density profile $\rho_{ml}(z)$, can then be written as

$$F_{ml}(z^*, E) = \sum_{j=1}^{N} f_j(z^*, E) \exp(-2\pi i z_j z^*) \propto \int \rho_{ml}(z) \exp(-2\pi i z z^*)\, dz. \quad (2)$$

The resonance diffraction effect in the intensity function $|F_{ml}(z^*, E)|^2$ from a system where the number of resonant atoms is only a small fraction of the total arises almost exclusively from the interference between those resonant atoms and the rest of the atoms in the structure (11, 13); this interference involves only the f'_j term for the resonant atoms. Furthermore, for a system with a centrosymmetric unit cell, such as the profile $\rho_{ml}(z)$ of our oriented SR multilayer samples (28, 24), this effective structure factor can then be written as

$$F_{ml}(z^*, E) = F_{ml}(z^*) + 2 \sum_{j=1}^{N_r} f'_j(z^*, E) \cos(2\pi z_j z^*) = F_{ml}(z^*) + F_{ml}^{res}(z^*, E), \quad (3)$$

where N_r is the total number of resonant atoms in the unit cell and $F_{ml}(z^*)$ and $F_{ml}^{res}(z^*, E)$ represent in turn the contribution to this total effective structure factor for the system from the nonresonant and the resonant atoms, where each have phase factors $\exp(i\phi[z^*])$ that have only ±1 values because $\phi(z^*) = 0, \pi$ only. As can be seen from the above, changes in the diffracted intensity $|F_{ml}(z^*, E)|^2$ with x-ray energy due to resonance effects should scale approximately linearly with $f'(E)$ for the resonant atoms. It follows from the characteristics of the x-ray absorption spectra of lanthanides about their L_{III} edges (12) that the resonance effects in $|F_{ml}(z^*, E)|^2$ will therefore be roughly symmetric as a function of energy with respect to the edge energy, E_{edge}, with the effects at positive ΔE with respect to E_{edge} being somewhat larger that those for negative ΔE.

Resonance diffraction data analysis

The first step in the analysis and interpretation of the data must be the calculation of $\rho_{uc}(z)$, the off-resonance electron density profile of the multilayer unit cell, from the corrected lamellar diffracted intensity $I_c(z^*, E)$. A General Fourier Synthesis Deconvolution (GFSD) method of analysis (29) was used to calculate the off-resonance, centrosymmetric $\rho_{uc}(z)$ from a typical lamellar intensity function $I_c(z^*, \text{edge} + 200eV)$.

Note that $\rho_{uc}(z)$ can be calculated from two intensity functions corresponding to different energies, and $\rho_{uc}^{res}(z)$, the electron density profile of the resonant atoms, can be obtained from the difference

$$\rho_{uc}(z, E) - \rho_{uc}(z, E'),$$

but for the analysis of the present resonance data, the more direct method described below proved more appropriate for reasons that will be discussed in Results. It follows from Eq. 3 that if the number of resonant atoms N_r is sufficiently small relative to N, the total number of atoms in the multilayer unit cell, thereby insuring that the phase factors of $F_{ml}(z^*, E)$ and $F_{ml}(z^*)$ are approximately the same, one can write (13) for the resonant contribution to the structure factor:

$$|F_{ml}^{res}(z^*)|^2 = |F_{ml}(z^*, \text{edge}) - F_{ml}(z^*, \text{edge} + \Delta)|^2$$
$$= [I_c^{1/2}(z^*, \text{edge}) - I_c^{1/2}(z^*, \text{edge} + \Delta)]^2, \quad (4)$$

where $F_{ml}(z^*, \text{edge})$ and $F_{ml}(z^*, \text{edge} + \Delta)$ represent the multilayer profile structure factors at the edge energy (E_{edge}) and another off-edge energy ($E_{edge} + \Delta$), and $I_c(z^*, \text{edge})$ and $I_c(z^*, \text{edge} + \Delta)$, represent the corresponding experimentally measured, corrected diffracted intensity functions. The structure factor modulus square of the resonant part of the structure can thereby be directly calculated from the appropriate intensity functions. If the corresponding phase factors $\exp[i\phi_{ml}^{res}(z^*)] = \pm 1$ for $F_{ml}^{res}(z^*)$ can be obtained, the electron density profile corresponding to just the resonant atoms is given directly by the Fourier transform of the phased resonant contribution to the multilayer structure factor:

$$\rho_{ml}^{res}(z) = \int |F_{ml}^{res}(z^*)| \exp[i\phi_{ml}^{res}(z^*)] \exp(-2\pi i z^* z)\, dz^*. \quad (5)$$

The modulus of the resonant contribution to the structure factor was then calculated according to Eq. 4, and the values of the corresponding phase function $\phi_{ml}^{res}(z^*)$, were determined using a constrained iterative refinement procedure (30) (see Results regarding the utility of that procedure for the analysis of this resonance data). Once $F_{ml}^{res}(z^*)$ and $\phi_{ml}^{res}(z^*)$ were obtained, $\rho_{ml}^{res}(z)$ was calculated directly via Eq. 5. Because this $\rho_{ml}^{res}(z)$ represents the profile of just the resonant atoms in the multilayers, the GFSD method of analysis was subsequently used to "deconvolute" $\rho_{ml}^{res}(z)$ to provide $\rho_{uc}^{res}(z)$. Finally, step-function electron density models (see Results) were used to model $\rho_{uc}^{res}(z)$ with a minimum number of discrete, localized metal binding sites. The adequacy of the models was tested by comparing the experimental vs. model $|F_{uc}^{res}(z^*)|^2$ and $\widetilde{\rho_{uc}^{res}(z)^2}$ functions, where $|F_{uc}^{res}(z^*)|^2$ is the modulus square of the resonant contribution to the unit cell structure factor, and $\widetilde{\rho_{uc}^{res}(z)^2}$ is the autocorrelation of the unit cell electron density profile of the resonant lanthanide atoms.

RESULTS

Observation of the resonance effect

All lamellar diffraction patterns $I_t(z^*, E)$ from a given SR multilayer sample were examined as described in the previous section to evaluate the stability of the multilayer, and to determine whether resonance effects existed for the stable multilayers. The magnitude of the resonance effects were large enough that they could be directly observed in arithmetic differences between patterns that had only been transformed to reciprocal space coordinate z^* and normalized to match their total intensities, and were otherwise uncorrected. However, observation of the characteristics (e.g., energy dependence) of the resonance effects was simplified if arithmetic differences were taken, instead, between the corresponding functions $I_t(z^*, E)$ integrated over identical, successive intervals Δz^* along z^*, to improve the statistics within each interval. Such difference intensity functions $\Delta I_t(z_k^*, E_{ij})$, where $z_k^* = (2k + \frac{1}{2})\Delta z^*$, $k = 0, 1, 2, \cdots$, are presented, for example, for two stable multilayer samples, (A) Tb^{3+}/protein molar ratio ~4, L_{III} edge (7,515 eV) ±50 eV; (B) La^{3+}/protein molar ratio ~4, L_{III} edge (5,484 eV) ±100 eV, in Fig. 1. Note how the z^*-dependence of the observed resonance effects is similar for the two different lanthanides, and how for a given sample the changes are symmetric around the edge (i.e., similar for $\pm\Delta E_{ij}$) and larger for larger ΔE_{ij}, and when $(E - E_{edge}) > 0$, as expected from the characteristic x-ray absorption spectra (and thereby $f'[E]$) for lanthanide L_{III} edges. Also note that the resonance effects are all substantially larger than the fluctuations present in the tests of multilayer stability. Fig. 2 shows the corresponding (A) uncorrected lamellar diffraction pattern $I_t(z^*, E)$ (La^{3+}/protein molar ratio ~4, L_{III} edge (5,484 eV) + 100 eV); (B) $\Delta I_t(z^*, \Delta E_{ij})$, the difference intensity function for E_i = 5,484 + 100 eV and E_j = 5,484 eV; and (C) $|F_{ml}^{res}(z^*)|^2$, the resonant contribution to the total multilayer profile structure factor, calculated according to Eq. 4.

GFSD analysis and calculation of the multilayer unit cell electron density profile $\rho_{uc}(z)$

To calculate the off-resonance unit cell-electron density profile $\rho_{uc}(z)$, a background scattering and Lorentz-corrected typical off-resonance lamellar diffraction pattern $I_c(z^*, E = 5{,}484 \pm 100 \text{ eV})$ (corresponding to the uncorrected pattern shown in Fig. 2 A) was subjected to GFSD analysis (29) as described in Methods. The GFSD method of analysis, developed previously for the analysis of the lamellar diffraction from multilayers presenting lattice and/or substitution disorder, uses a set of parameters characterizing the multilayer lattice and profile structure factor phase functions (the phase function can only have values of 0 or π, due to the centrosymmetric nature of the unit cell profile). Such parameters are optimized by iteratively minimizing the least squares difference between the GFSD-calculated and the experimentally determined intensity ($I_c[z^*]$) and autocorrelation $\widetilde{\rho_{ml}(z)^2}$ functions. Fig. 3 shows those resulting functions (Fig. 3, A and B), as well as the calculated unit cell structure factor modulus square $|F_{uc}(z^*)|^2$ (Fig. 3 C), and unit cell electron density profile $\rho_{uc}(z)$ (Fig. 3 D), calculated to a low spatial resolution of ~40 Å, for a

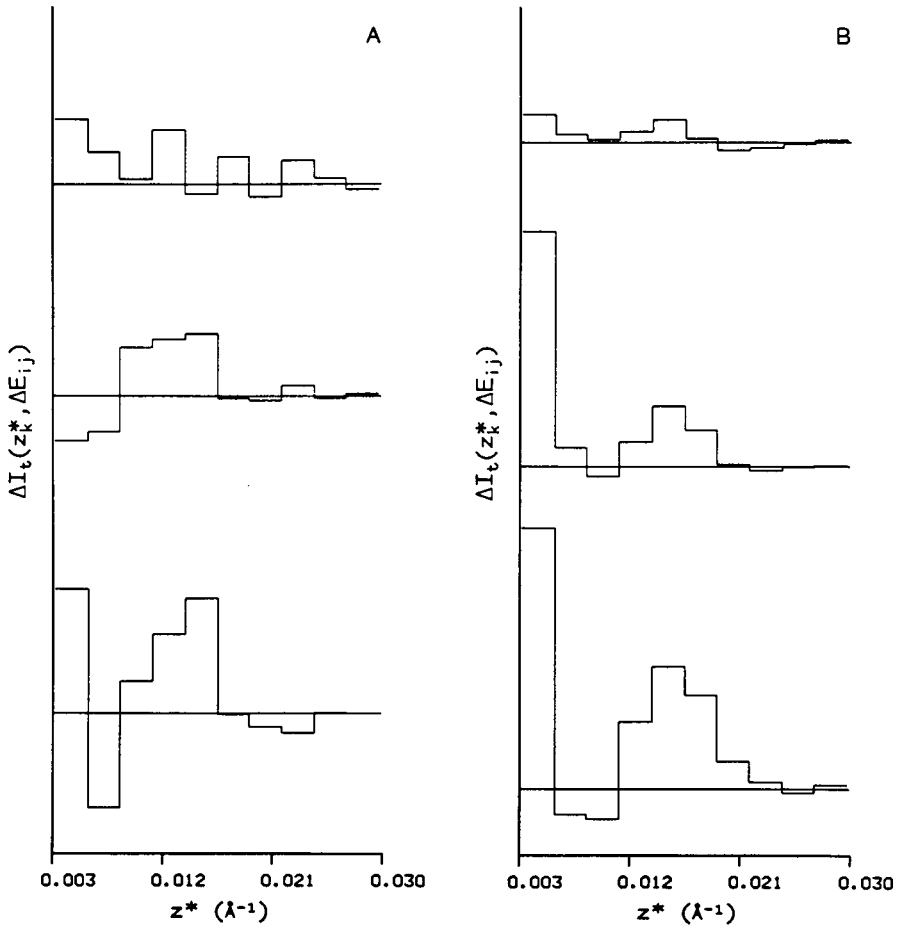

FIGURE 1 Difference intensity functions $I_t(z_k^*, \Delta E_{ij})$, between uncorrected intensity functions integrated over identical, successive intervals Δz^*. Data were collected for 1,800 s at each of three different energies in the following order: L_{III} edge (1), L_{III} edge-ΔE, L_{III} edge + ΔE, and L_{III} edge (2). Fig. 1 *A* corresponds to a sample with Tb^{+3}/protein molar ratio ~4, and ΔE = 50 eV. Fig. 1 *B* corresponds to a sample with La^{+3}/protein molar ratio ~4, and ΔE = 100 eV (the vertical scale in Fig. 1 *B* is roughly half that in Fig. 1 *A*). At the top of each figure, the difference between the two L_{III} edge intensity functions for the sample, $\Delta E_{i=j}$ = [L_{III} edge (1) − L_{III} edge (2)] is shown. The difference $\Delta E_{i\neq j}$ = [(L_{III} edge −ΔE) − L_{III} edge (2)] is shown in the middle, and at the bottom of the figures, the difference $\Delta E_{i\neq j}$ = [(L_{III} edge + ΔE) − L_{III} edge (2)] is presented. See text for details.

multilayer lattice periodicity D = 221 Å. Several features of these results deserve mention. Both the calculated and experimental autocorrelation functions $\rho_{ml}(z)^2$ are essentially featureless beyond the calculated lattice periodicity of 221 Å, and the intensity functions $I_c(z^*)$ resemble closely the unsampled shape of the calculated unit cell structure factor modulus square $|F_{uc}(z^*)|^2$. These facts, as well as the presence of only weak lamellar diffraction for $z^* > 1/40$ Å, are indications of the presence of a large degree of lattice disorder in these multilayers, arising from the absence of strong unit-cell-to-unit-cell correlations. The lamellar diffraction therefore arises essentially from independently scattering unit cells, i.e., $I_c(z^*, E) \propto |F_{uc}(z^*)|^2$. Furthermore, examination of the GFSD-calculated intensity function suggests the presence of a weak second-order diffraction maximum at $z^* \sim 0.0082$ Å that is at best only partially resolved in the experimental data (see Fig. 3 *A*). The lamellar intensity function in this region of z^* is affected by the Δz^* resolution and the background scattering correction, but fortunately this does not significantly affect the GFSD results providing $\rho_{uc}(z)$ off-resonance, because this second-order maximum is very weak compared with the other maxima in the diffraction pattern.

Phasing of $|F_{ml}^{res}(z^*)|$ and calculation of $\rho_{uc}^{res}(z)$

The resonant contribution to the structure factor, $|F_{ml}^{res}(z)|$, was calculated according to Eq. 4, from the

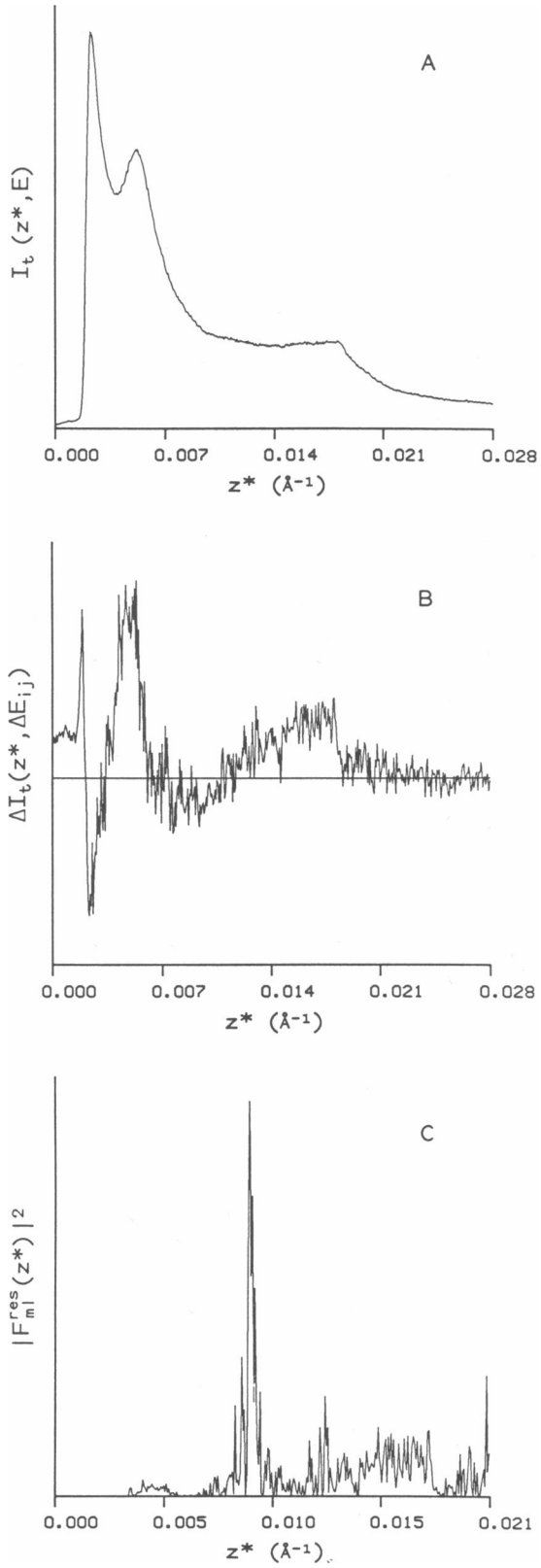

appropriate background-corrected[1] lamellar intensity functions. As indicated previously, phasing of $|F_{ml}^{res}(z^*)|$ permits the direct calculation of the electron density profile of the resonant lanthanide atoms using Eq. 4. $|F_{ml}^{res}(z^*)|$ is shown in Fig. 2 *C*, calculated as the difference

$$[I_c^{1/2}(z^*, \text{edge}) - I_c^{1/2}(z^*, \text{edge} + 100\,eV)].$$

Note that both $|F_{ml}^{res}(z^*)|^2$ and the corresponding $\Delta I_t(z^*, E_{ij})$ of Fig. 2 *B* are significantly different from zero in the region corresponding to the position of the weak second-order diffraction maximum in the intensity function $I_e(z^*, \text{edge} + 100\text{ eV})$, and also that $\Delta I_t(z^*, E_{ij})$ changes sign over the region containing the unresolved first- and second-order maxima in $I_c(z^*, E)$, which are assigned a constant phase in the GFSD analysis of $I_c(z^*, \text{edge} + 100\text{ eV})$. Because of this consideration $(|F_{ml}^{res}[z^*]|^2$ has important features in a region where $I_c(z^*, E)$ have only a very weak, partially resolved second-order maximum that can not be phased in the GFSD analysis of the off-resonance $I_c[z^*, E]$), the phases determined for the off-resonance $I_c(z^*, E)$ cannot be directly applied to $|F_{ml}^{res}(z^*)|$, which must therefore be phased independently. Hence, $|F_{ml}^{res}(z^*)|$ was phased using an iterative "box refinement" algorithm (30) as indicated in Methods. Application of this box refinement technique (which iteratively converges to an allowed phase function for a profile structure, based on information related to the finite extent of the profile structure contained in $I_c[z^*]$) was possible due to the large amount of lattice disorder present in the multilayer samples (see previous subsection). The box refinement algorithm was given several "trial" phase functions with vastly different characteristics. Independently of the initial "trial" phase function, the method converged to a single final phase function that assigned alternate phases of ~ 0 or π to the successive regions of constant phase in $|F_{ml}^{res}(z^*)|$. This is illustrated in detail in Fig. 4. The resulting final resonant atom electron density profile functions for the multilayer, $\rho_{ml}^{res}(z)$, were also consis-

FIGURE 2 Examples of the various functions involved in the analysis of the resonance x-ray diffraction data. (*A*) Typical uncorrected, off-resonance lamellar intensity function $I_t(z^*, E)$, for E = [La L_{III} edge + 100 eV]. (*B*) Typical difference intensity function $\Delta I_t(z^*, \Delta E_{ij})$ for $\Delta E_{i \neq j}$ = [(La L_{III} edge + 100 eV) − La L_{III} edge] that shows the changes in the continuous lamellar diffracted intensity function due to the resonance effect (this continuous difference function corresponds to the integrated difference function $\Delta I_t(z_k^*, \Delta E_{ij})$ shown in Fig. 1 *B*). (*C*) $|F_{ml}^{res}(z^*)|^2$, the corresponding resonant contribution to the structure factor modulus for the multilayer profile, calculated according to Eq. 4. See text for details.

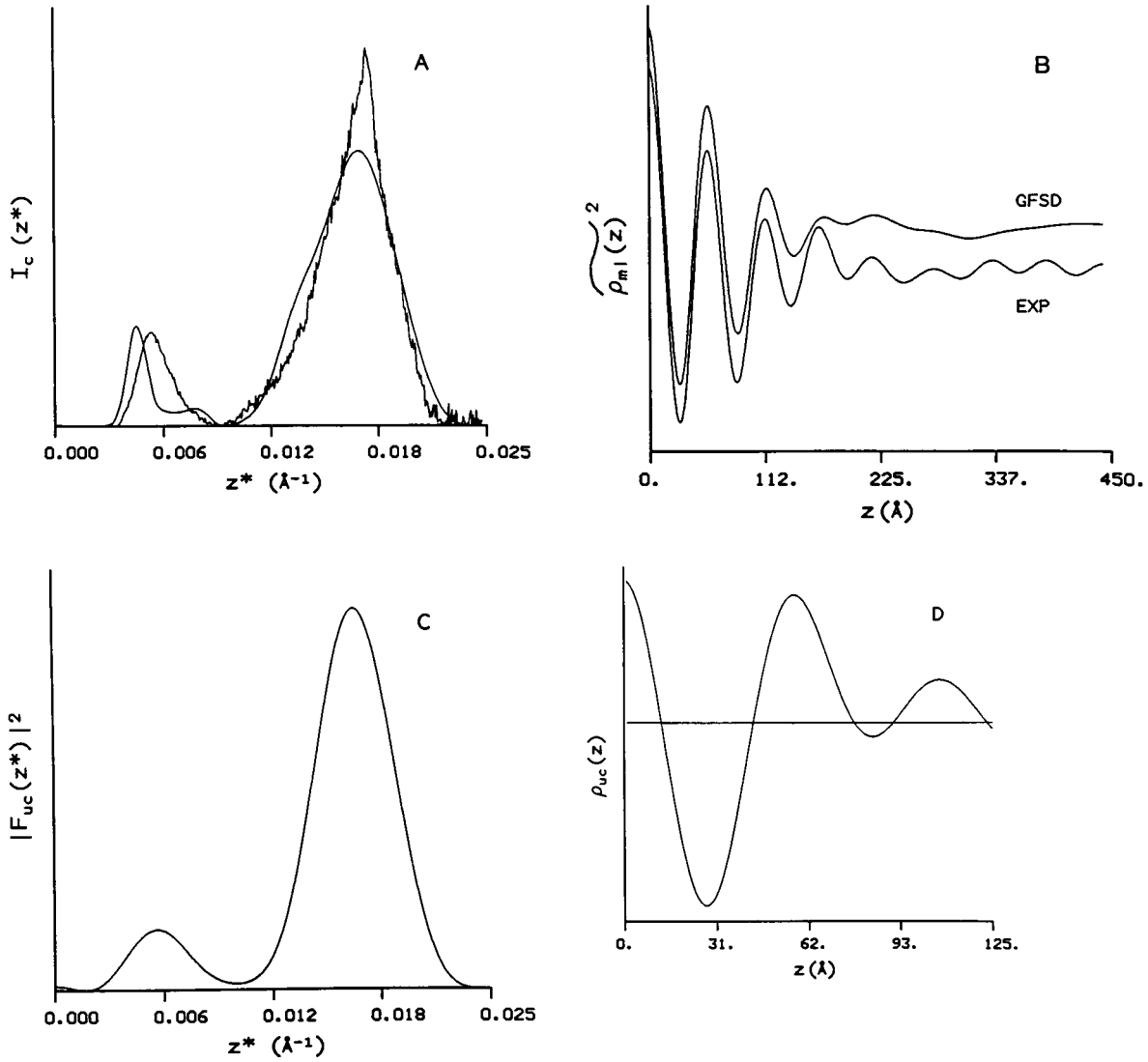

FIGURE 3 General Fourier Synthesis Deconvolution (GSFD) analysis of the off-resonance lamellar intensity functions to calculate the off-resonance multilayer unit cell electron density profile, $\rho_{uc}(z)$. (*A*) GFSD-calculated (*smooth*) and experimental lamellar intensity functions $I_c(z^*)$. Note the presence in the calculated function of a weak, partially resolved second order diffraction maximum at $z^* \sim 0.0082$ Å^{-1}, that is not observable in the experimental function, probably due to insufficient Δz^* resolution, complicated by the lamellar background correction at low z^*. See text for details. (*B*) GFSD-calculated (*top*) and experimental multilayer profile autocorrelation functions, $\tilde{\rho}_{ml}(z)^2$. Note that both functions are essentially featureless for values of z larger than the calculated multilayer lattice periodicity $D \sim 221$ Å. (*C*) GFSD-calculated unit cell profile structure factor modulus square $|F_{uc}(z^*)|^2$. Notice that the intensity functions shown in *A* closely resemble the structure factor modulus square. (*D*) GFSD-calculated, low-resolution (40 Å) unit cell electron density profile $\rho_{uc}(z)$, containing the SR single membrane profile within $0 \leq |z| \leq D/2 \sim 110$ Å. See text for details.

tently similar for all initial trial phase functions. Because the box refinement analysis contains no assumptions about the symmetry of the profile structure, the final phase functions have values that are not exactly 0 or π, but which nevertheless clearly indicate the correct values for a centrosymmetric profile structure.

Once the correct phase function $\phi_{ml}^{res}(z^*)$ for $|F_{ml}^{res}(z^*)|$ had been calculated, it was used in conjunction with GFSD analysis to calculate the centrosymmetric electron density profile of the resonant metal atoms for just the multilayer unit cell, $\rho_{uc}^{res}(z)$. The results obtained from the GFSD analysis, as well as a typical electron density profile obtained from the box refinement calculations are shown in Fig. 5. As expected, both methods of

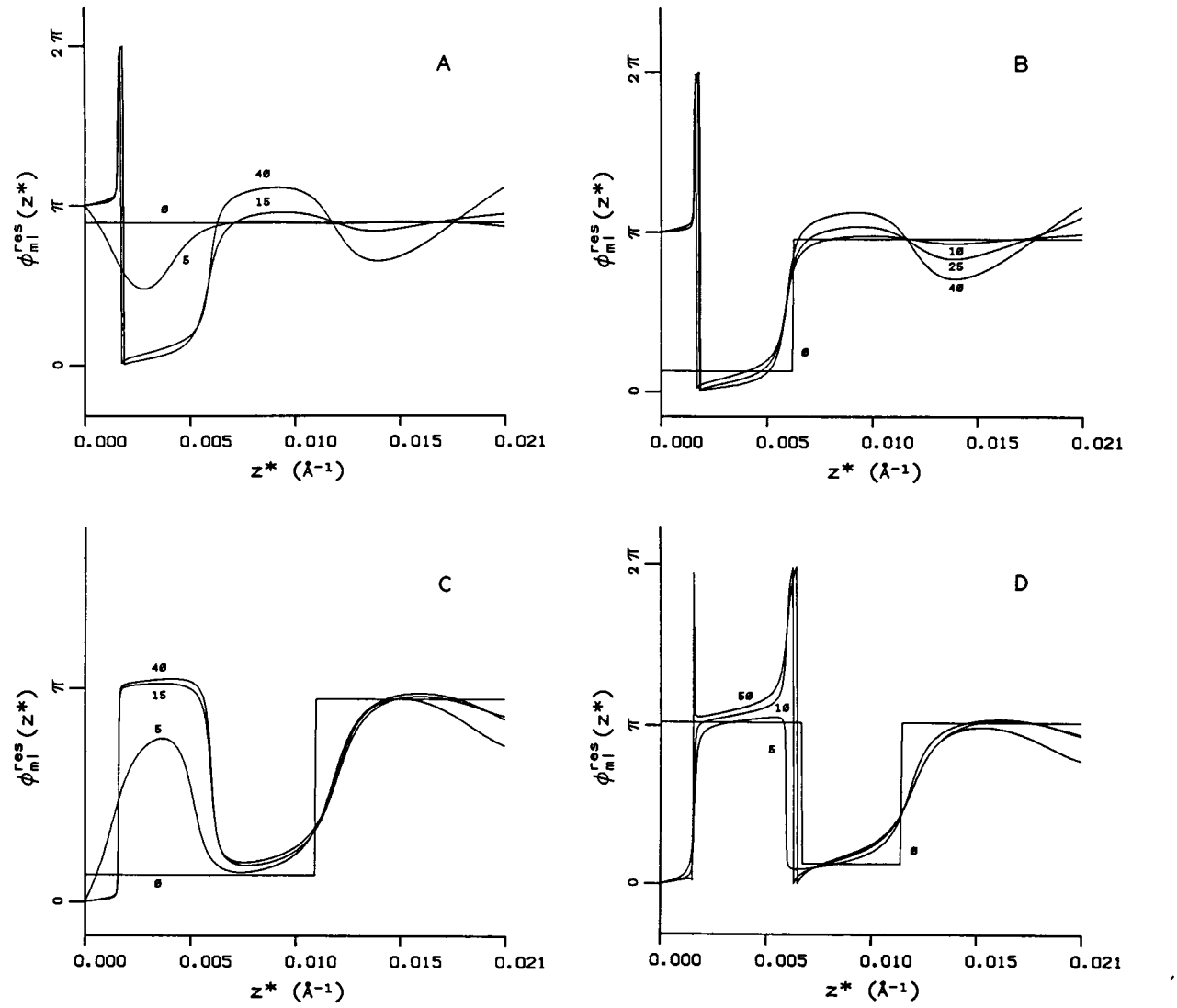

FIGURE 4 Box refinement analysis used to determine the appropriate phases $\phi_{ml}^{res}(z^*)$ for the resonant contribution $|F_{ml}^{res}(z^*)|$ to the total multilayer profile structure factor (see Fig. 2 *C*). As the iteration number (indicated by the small numeral next to the different graphs) increases, the calculated phase function $\phi_{ml}^{res}(z^*)$ becomes progressively more different from the initial "trial" phase function (expressed as a step-function), and converges to its final form. Note that independently of the vastly different characteristics of the various initial "trial" phase functions, the method always converged to a final phase function that assigned alternate phases of ~ 0 or π to the successive maxima, i.e., regions of constant phase in $|F_{ml}^{res}(z^*)|^2$.

analysis produced $\rho^{res}(z)$ functions that are very similar within the unit cell, namely $|z| \leq D/2 \sim 110$ Å.

Modeling of $\rho_{uc}^{res}(z)$

To facilitate the interpretation of the low-resolution continuous electron density profile corresponding to the resonant lanthanide atoms, the continuous profile was fitted with step-function electron density models (31, 32) to represent a small number of discrete, localized metal binding sites in the unit cell profile. The guiding principles used for constructing the models were the following. First, we sought the minimum possible number of discrete metal sites necessary to model the continuous profile. Secondly, we sought the minimum step width for each site used to represent metal electron density (i.e., assuming highly localized metal binding sites in the unit cell profile). Finally, at every stage of the modeling process, the adequacy of the model was tested via comparison of the model vs. experimental resonant unit

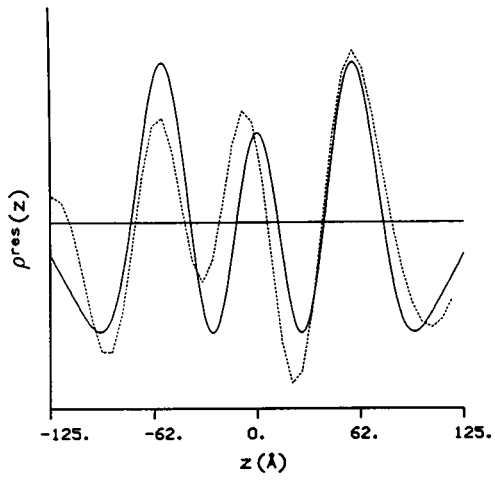

FIGURE 5 Electron density profile of the resonant lanthanide atoms calculated by the GFSD method $\rho_{uc}^{res}(z)$ (*solid line*) and box refinement analysis $\rho_{ml}^{res}(z^*)$ (*dotted line*). Note the similarity between these two functions within the multilayer unit cell $|z| \leq D/2 \sim 110$ Å. See text for a discussion of these results.

cell structure factor modulus square $|F_{uc}^{res}(z^*)|^2$, and unit cell metal electron density profile autocorrelation function $\widetilde{\rho_{uc}^{res}}(z)^2$. The number of localized metal sites in the model profile was progressively increased from one to three sites per single membrane profile within $0 \leq |z| \leq D/2 \sim 110$ Å (or up to six sites in the apposed membrane pair that forms the unit cell profile within $-D/2 \leq z \leq +D/2$). The results from the modeling calculation can be summarized as follows. A single localized metal binding site per membrane profile, best modeled using a 5-Å wide electron density step centered at $z = 61$ Å, is sufficient to correctly reproduce the number as well as the position of the maxima in both $|F_{uc}^{res}(z^*)|^2$ and $\widetilde{\rho_{uc}^{res}}(z)^2$. However, the amplitudes of the different maxima in both functions are obviously not correct[2] ($R_F = 1.626 \times 10^{-1}$; $R_\rho = 2.486 \times 10^3$). See Fig. 6. Addition of a second localized metal binding site per membrane profile, best modeled with a 5-Å wide step centered at $z = 2.5$ Å (such that the two steps in the apposed single membrane profiles that form the unit cell profile produce a single 10-Å wide step centered at $z = 0$(Å), correctly reproduces virtually all the features in $|F_{uc}^{res}(z^*)|^2$ and $\widetilde{\rho_{uc}^{res}}(z)^2$ ($R_F = 1.015 \times 10^{-2}$; $R_\rho = 1.528 \times 10^2$). The results obtained with this second model are also shown in Fig. 6. If a third site per membrane profile is added (best modeled with a 5-Å wide step centered at $z = 50$ Å), the site formerly centered at $z = 61$ Å moves out to $z = 63$ Å, and a nearly perfect fit is obtained for both test functions, with some improvement over the two site per membrane profile model, especially at low z^* and large z ($R_F = 9.317 \times 10^{-3}$; $R_\rho = 1.413 \times 10^2$, figures not shown).

[2]The residuals for a given function $f(x)_{calc}$ were calculated as:

$$R_f = \Sigma [f(x)_{calc} - f(x)_{exp}]^2 / \Sigma [f(x)_{exp}]^2.$$

DISCUSSION

Interpretation of the low-resolution, off-resonance membrane profile

Only a limited amount of information can be obtained directly from the low-resolution (40 Å) electron density profile for a single SR membrane presented in Fig. 3 *D*. The positions of the maxima in the continuous profile are largely determined by the spatial resolution of the data, and do not correspond to the positions of any specific molecular or submolecular features in the actual membrane electron density profile. Comparison of the off-resonance, low-resolution SR membrane electron density profile obtained in this study with other low-resolution SR membrane profiles obtained under similar experimental conditions, but for which substantially higher resolution data has been analyzed is very informative, particularly if considered in combination with the results obtained from the modeling of $\rho_{uc}^{res}(z)$. Such a comparison is made in Fig. 7. The pair of low-(35 Å)/high-(13 Å) resolution membrane electron density profiles shown in Fig. 7 *A* corresponds to a multilayer sample prepared under conditions (low [<40 μM] $[Ca^{+2}]$, $[Mg^{+2}]$; same relative humidity and temperature) comparable to those used in the present study. In Fig. 7 *B*, the low-resolution profile from Fig. 7 *A*, and the low-resolution profile calculated in the present study are superimposed. Note how these two low-resolution profiles are very similar. In Fig. 7 *A*, note that the maximum at $z \sim 59$ Å in the low-resolution profile actually encompasses two maxima in the corresponding high-resolution profile, the first of which (at $z \sim 50$ Å) corresponds to the position of the phospholipid polar head groups on the extravesicular side of the membrane (8). The results shown in Fig. 7 indicate that the off-resonance, low-resolution electron density profile for the SR membrane calculated for the samples analyzed in the present study appears as a "normal" low-resolution SR membrane profile; the EGTA treatment and the subsequent addition of a low concentration (<50 μM) of lanthanide (III) ion did not cause any drastic changes in the profile structure of the SR membrane. In particular, the region of the membrane profile containing the phospholipid bilayer ($0 \leq z \leq 59$ Å in the low resolu-

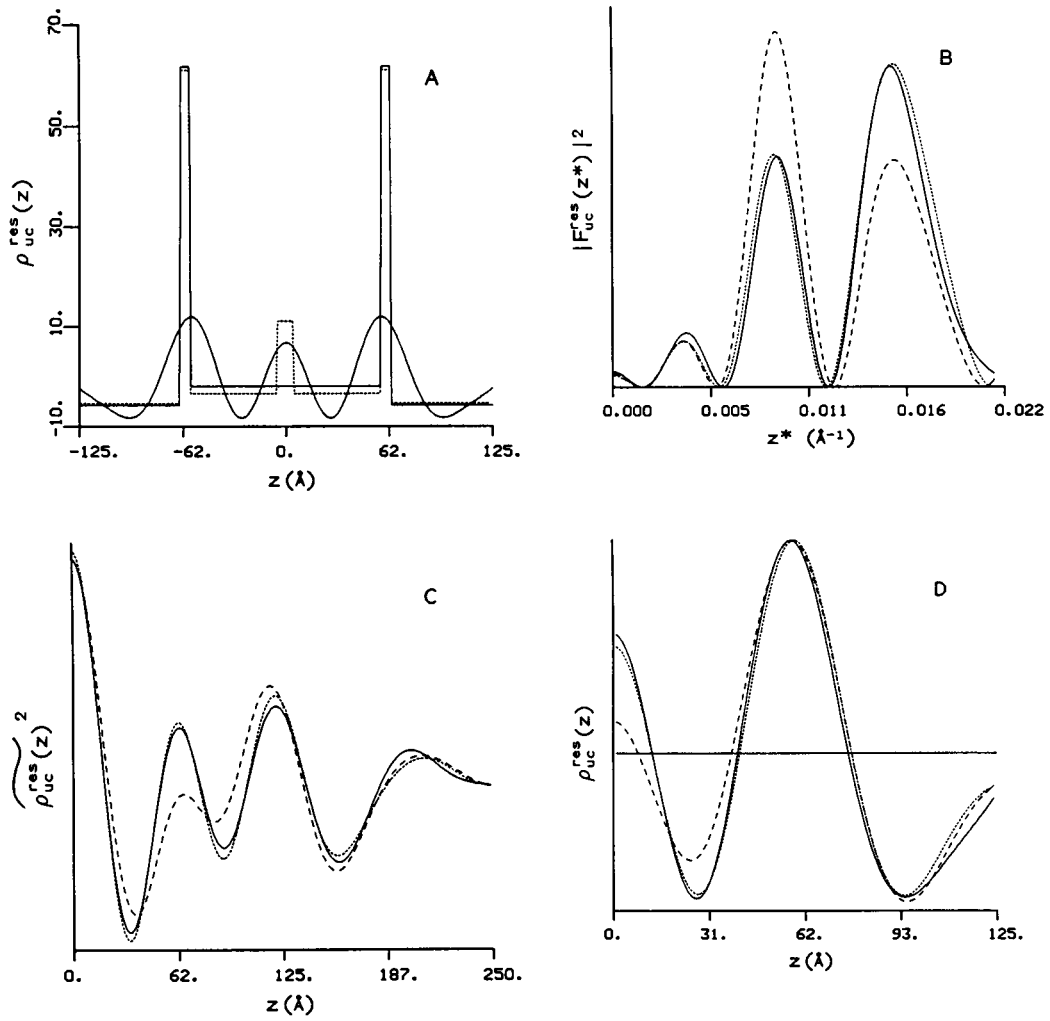

FIGURE 6 Modeling the resonant atom unit cell electron density profile $\rho_{uc}^{res}(z)$, using a step-function model with one vs. two localized metal binding sites per single membrane profile. The best single-site model contained a 5-Å wide step centered at $z = 61$ Å. A second site was best modeled with a 5-Å wide step centered at $z = 2.5$ Å. (*A*) Continuous experimental profile $\rho_{uc}^{res}(z)$, and the best one-site (*solid line*) and two-site (*dotted line*) step-function models. (*B*) Experimental (*solid line*) and best model unit cell structure factor modulus squares $|F_{uc}^{res}(z^*)|^2$. (*C*) Experimental (*solid line*) and best model unit cell profile auto-correlation functions $\rho_{uc}^{res}(z)^2$. (*D*) Experimental (*solid line*) $\rho_{uc}^{res}(z)$ and the best model represented as a continuous electron density profile (obtained via double Fourier transformation at 40 Å resolution). Note that this best single-site model accounts for all the basic features of the functions $|F_{uc}^{res}(z^*)|^2$ and $\rho_{uc}^{res}(z)^2$ used to test the adequacy of the model (*solid vs. dashed lines in B–D*), but does not produce a particularly good fit to the experimentally determined functions ($R_F = 1.626 \times 10^{-1}$; $R_\rho = 2.486 \times 10^3$). The fit of the model to the experimental test functions (*solid vs. dotted lines in B–D*) is significantly improved by the addition of a second site ($R_F = 1.015 \times 10^{-2}$; $R_\rho = 1.528 \times 10^2$). See text for a discussion of these results.

tion profiles) was not affected. Furthermore, the lamellar diffraction patterns of this study do not show the characteristics typical of lipid lateral phase separation (26, 32, 33). The preceeding observations indicate that the phospholipid polar headgroups on the extravesicular side of the membrane profile for the samples used for the present work are most likely also located at $z \sim 50$ Å, as for the similar low-/high-resolution electron density profiles shown in Fig. 7 *A*.

Step-function modeling of $\rho_{uc}^{res}(z)$

Some aspects of the modeling process for the low-resolution, continuous electron density profile of the resonant metal atoms $\rho_{uc}^{res}(z)$, particularly those related to the widths and positions of the steps used to represent discrete, localized metal electron density, require some discussion. In constructing the step-function models of continuous electron density profiles, the minimum width

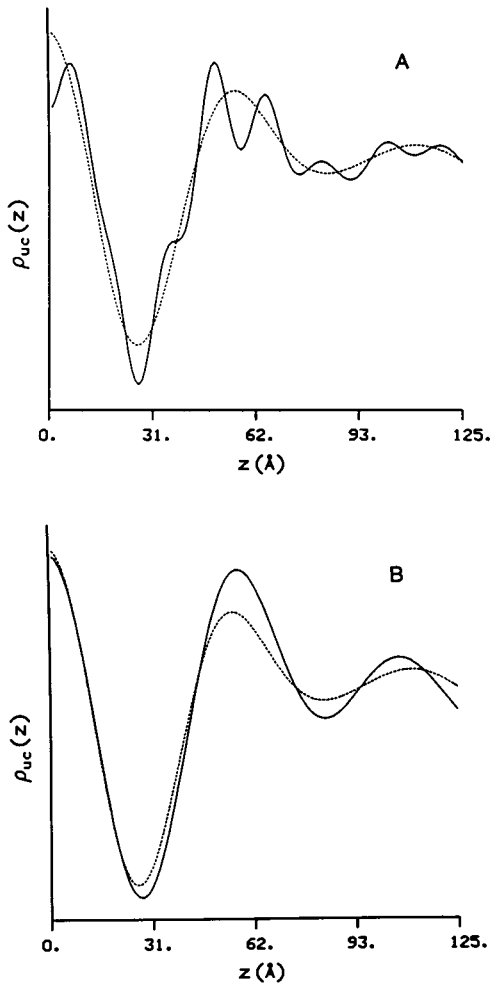

FIGURE 7 Interpretation of the off-resonance, low-resolution (40 Å) SR membrane electron density profile $\rho_{uc}(z)$ for $0 \leq z \leq D/2 \sim 110$ Å. (*A*) High-resolution membrane electron density profile (*solid line*, 13 Å resolution) for a SR multilayer sample under experimental conditions very similar to those used in the present study, and the corresponding low-resolution profile (*dotted line*, 35 Å). (*B*) Off-resonance, low-resolution membrane electron density profile calculated from the data of the present study (*solid line*, 40 Å), and low-resolution profile from *A* (*dotted line*). Note that both low-resolution membrane profiles are very similar, especially over the region containing the phospholipid bilayer ($0 \leq |z| \leq 59$ Å). See text for further discussion.

of the steps in the model is usually chosen to be comparable to the spatial resolution to which the continuous profile was calculated. In our models, steps up to 40 Å wide (the resolution of the continuous profile) can be used to represent all metal sites, and indeed, the low resolution of our data alone does not justify the use of narrower steps. However, physico-chemical considerations, as well as considerations concerning the type of information that we sought from the model calculations led us to use narrow steps (5 Å) to represent the electron density of the resonant lanthanide atom sites in the membrane profile. Only a relatively small concentration of lanthanide (III) ions was present in our samples (~ 4 lanthanide [III] ions/protein molecule), and it is known that there are specific metal binding sites in the SR membrane (e.g., sites in the Ca^{+2} ATPase protein, and phospholipid polar head groups) where the lanthanide ions will bind with relatively high affinity ($K_a \geq 10^4 - 10^5$ [34]). It therefore seemed unreasonable to expect the few lanthanide ions present in the oriented SR membrane multilayer to bind frequently enough to result in a continuous distribution of metal density over extended portions of the membrane profile. Not only is the lanthanide concentration in the multilayer too low to produce the necessary statistical distribution, but one would also have to assume that sites that bind the lanthanide ions with an affinity at least comparable to that displayed by the phospholipid polar headgroups ($K_a > 10^4 - 10^5$) are distributed continuously over extended portions of the membrane profile. The small width of the steps used in our best models should only be taken as evidence that (in agreement with what one would expect based on the independent physico-chemical considerations just presented above) the low-resolution continuous electron density profile of the resonant lanthanide atoms $\rho_{uc}^{res}(z)$ is consistent with, and can be fully explained by assuming that the metal atoms are specifically bound to a very small number (≤ 3) of discrete, localized sites in the single membrane profile.

The allowable step-function electron density models are very sensitive to variations in the positions of the centers of mass of the steps. The sensitivity of the model to changes in the position of a particular step is, in general, directly proportional to the relative electron density assigned to that step. Changing the position of the center of mass of a step by an amount much smaller (e.g., 1–2 Å) than the resolution limit (~ 40 Å) of the continuous profile being modeled causes dramatic changes in the positions and amplitudes of the maxima in the functions ($|F_{uc}^{res}[z^*]|^2$ and $\rho_{uc}^{res}[z]^2$) used to test the adequacy of the model. Based on the sensitivity of the test functions to changes in the step function models, we estimate that the approximate accuracy to which the positions of the centers of the mass of the discrete, localized metal binding sites in the membrane profile were determined is about ± 1–2 Å. Note that making the assumption that the metal binding sites are discrete and localized in the membrane profile provides a powerful constraint, allowing the modeling of $\rho_{uc}^{res}(z)$ to locate the sites to an accuracy much higher than what would seem possible given the limited spatial resolution of the diffraction data. In addition, note that because $\rho_{uc}^{res}(z)$ represents only electron density from the resonant

lanthanide atoms, the relative areas of the electron density steps in the models are a direct measurement of the relative amounts of lanthanide bound to each discrete, localized binding site in the membrane profile.

Interpretation of the modeling of $\rho_{uc}^{res}(z)$

As indicated above, modeling of the low-resolution resonant metal atom electron density profile, based on the assumption that the metal binding sites in the membrane profile are discrete and localized, indicates that the characteristics of the continuous profile from the resonance x-ray diffraction data can be fully explained by assuming that the lanthanide (III) ions bind to a maximum of three sites in the single membrane profile. Combining this result with the off-resonance, high-resolution (13 Å) electron density profile for the SR membrane, and its decomposition into the separate profiles of the membrane's molecular components (8), provides the following scenario. The most basic features of the derived $\rho_{uc}^{res}(z)$ can be explained by assuming binding of the lanthanide (III) ions to a single localized site in the SR membrane profile. This site is centered at $z = 61 \pm 2$ Å (see Fig. 6). Examination of the derived off-resonance electron density profile for the SR membrane (see Figs. 3 *C* and 7), as well as consideration of the known position of the phospholipid bilayer within this profile (8) indicates that the phospholipid polar headgroups on the extravesicular side of the membrane profile are centered at a significantly smaller value of the z coordinate, namely about $z = 50$ Å. Therefore, the discrete binding site at $z \sim 61$ Å definitively located outside the lipid bilayer, in the portion of the Ca^{+2} ATPase protein that protrudes from the phospholipid bilayer into the extravesicular space (8).

Addition of a second site per membrane profile (centered at $z \sim 2.5$ Å), located at the intravesicular edge of the membrane, causes a marked improvement in the model (see Fig. 6). In terms of the molecular components of the SR membrane, the position of the second site in the model corresponds to the position of the phospholipid polar headgroups and the portion of the ATPase protein located in that region on the intravesicular side of the membrane profile. Based on the relative areas of the steps in the model (that are proportional to the amount of metal at the corresponding site, see previous subsection), almost 87% of the lanthanide ions are bound to the first site on the protein, and only 13% are bound to the second site located on the intravesicular side of the membrane profile. Addition of a third site, centered at $z \sim 50$ Å, a position in the membrane profile that corresponds to that of the extravesicular phospholipid polar headgroups, and the portion of the ATPase protein located in that region, causes a significant but smaller improvement in the model. Addition of this third site also causes the site previously centered at $z \sim 61$ Å to shift outward to $z \sim 63$ Å. Most of the lanthanide ions (77%) are still bound to the (exclusively) protein site at $z \sim 63$ Å, with only 23% of them bound to the other two sites in the single membrane profile. Interestingly, although some metal density on the third, lowest-occupancy site centered at $z \sim 50$ Å causes an improvement of the model, addition of more metal to this site dramatically worsens the fit. This provides further evidence that the site centered at $z \sim 63$ Å does not correspond to the extravesicular phospholipid polar headgroups, and that indeed most of the lanthanide ions are actually bound to the Ca^{+2} ATPase protein.

A reasonable assumption is that the lanthanide (III) ions on the sites centered at $z \sim 2.5$ Å and $z \sim 50$ Å are bound to the intravesicular and extravesicular phospholipid polar head groups, respectively. The equilibrium constant for binding of lanthanide (III) ions to acidic (negatively charged) phospholipid headgroups is in the range $10^4 < K_a < 10^5$ (34). Given the relative occupancies of the three sites, the metal binding site centered at $z \sim 63$ Å must have an association constant for lanthanide (III) ion binding approximately an order of magnitude larger than that for the phospholipid polar headgroups, namely in the range $10^5 < K_a < 10^6$. The presence of metal density on the intravesicular surface of the closed SR membrane vesicles indicates that after 15–20 h (the amount of time that the vesicles had been exposed to lanthanide before the resonance diffraction experiment), some lanthanide ions permeated the membrane. While it is not known if the lanthanide distribution reflected by the lanthanide electron density profile represents an equilibrium distribution, the obtained distribution does indicate (again assuming that the lanthanide [III] ions at the sites centered at $z \sim 2.5$ Å and $z \sim 50$ Å are bound to the phospholipid polar head groups) that there seems to be more anionic and zwitterionic phospholipid headgroups (to which lanthanides also bind [35]) in the intravesicular lipid monolayer than in the extravesicular monolayer of the isolated SR membrane vesicles. It has been reported (8, 36) that phospholipids are so asymmetrically distributed in the inner and outer phospholipid monolayers of isolated SR membrane vesicles, with respect to the nature of both their headgroups and their aliphatic chains.

The metal binding site centered at $z \sim 63$ Å is located in what is known as the "stalk" portion of the "headpiece" of the rotationally averaged profile structure of the Ca^{+2} ATPase protein (8). The localized nature of the site, the apparent magnitude of the equilibrium constant

for lanthanide (III) ion binding at this site, as well as the results from a large number of the previous experiments (that indicate that lanthanide [III] ions compete with Ca^{+2} for high-affinity binding sites in the protein (16–18), that lanthanide [III] ions displace Ca^{+2} from specific sites in the Ca^{+2} ATPase with diphasic kinetics attributable to sequential exchange, and activate phosphorylation of the Ca^{+2} ATPase by ATP [19]) lead us to believe that the metal binding site located by this study in the "stalk" portion of the Ca^{+2} ATPase protein "headpiece" could also be a high-affinity binding site for Ca^{+2} involved in the active transport of this ion across the SR membrane.

The final result of the modeling of $\rho_{uc}^{res}(z)$, the resonant atom unit cell electron density profile, is shown in Fig. 8, along side a schematic representation of the Ca^{+2} ATPase protein in the SR membrane. The rotationally averaged profile structure of the protein was directly determined via x-ray and neutron diffraction studies (8), for the E_1 conformation of the enzyme in the presence of Ca^{+2}, and high (10 mM) Mg^{+2} concentration. As shown in Fig. 7, the low-resolution SR membrane electron density profile calculated from the data in this study is very similar to that observed in the absence of La^{+3} for comparable temperature and low $[Mg^{+2}]$ conditions. The schematic protein profile structure shown in Fig. 8 is the same as that calculated in reference 8, except that the shape of the protein headpiece was modified slightly to account for the increase in the length of the "stalk" of the headpiece observed under low $[Mg^{+2}]$ conditions (33). The putative secondary/tertiary structure of the protein predicted on the basis of its primary sequence (6, 7) agrees with the profile structure derived from the x-ray and neutron diffraction data.

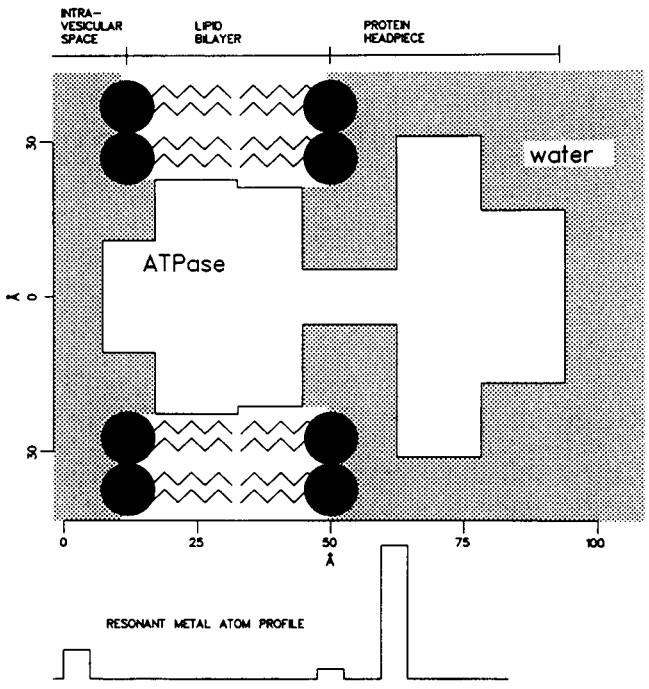

FIGURE 8 Position and relative occupancy of the high-affinity metal binding sites in the SR membrane profile structure, shown as the resonant metal atom profile. The separate, cylindrically averaged Ca^{+2} ATPase protein profile shown schematically, scaled and positioned in the membrane lipid bilayer, was calculated (8) from x-ray and neutron diffraction studies, and agrees with the putative secondary/tertiary structure for the Ca^{+2} ATPase predicted on the basis of its primary sequence. See text for details.

The recent results concerning the effects of site-specific mutagenesis on Ca^{+2} transport and activation of the Ca^{+2} ATPase (9, 10), combined with the putative secondary/tertiary structure of the enzyme predicted on the basis of its primary sequence (6, 7), have suggested the identification of a Ca^{+2} binding site associated with enzyme activation, located within the transmembranous region of the putative structure. A second Ca^{+2} binding site involved in Ca^{+2} transport but not essential for enzyme activation, was similarly identified within the "stalk" region of the putative structure. The suggested location of this second site is in agreement with the present work, and the results of fluorescence energy transfer measurements (19, 37). However, it has been shown that lanthanide (III) ions activate the ATPase function of the enzyme, and displace Ca^{+2} with kinetics that suggest sequential exchange of Ca^{+2} by La^{+3}. A calcium-resonance x-ray diffraction experiment should significantly contribute to clarify the actual location of the calcium binding sites in the Ca^{+2} ATPase profile structure. We are currently working on the design and realization of such an experiment.

CONCLUSION

These resonance x-ray diffraction studies of oriented multilayers of isolated SR membrane vesicles containing a low concentration of La(III) or Tb(III) ions (lanthanide/protein molar ratio ~ 4) have enabled us to calculate the off-resonance membrane electron density profile and the separate electron density profile of the resonant lanthanide atoms bound to the membrane, both to a low spatial resolution of ~ 40 Å. Comparison of this low-resolution electron density profile for the SR membrane with a higher (13 Å) resolution profile derived separately for the SR membrane under approximately equivalent experimental conditions, and modeling of the low-resolution lanthanide electron density profile with step-function model profiles based on the assumption of discrete, localized metal binding sites in the membrane profile, indicated that the lanthanide

(III) ions bind to a maximum of three sites in the SR membrane profile. The positions of two of these sites correspond to the two regions containing the polar headgroups of the lipid bilayer within the SR membrane profile, and could indicate binding of lanthanide (III) ions either to the phospholipid polar head groups themselves, or to the portion of the Ca^{+2} ATPase protein also located within those two regions of the membrane profile. The third site, where most (~80%) of the lanthanide ions are bound, is located in the "stalk" portion of the "headpiece" of the profile structure of the Ca^{+2} ATPase protein, some 12 ± 2 Å outside the position of the phospholipid polar headgroups on the extravesicular membrane surface. Binding of lanthanide (III) ions to this high-affinity binding site seems to occur with an affinity roughly an order of magnitude larger than that for binding to acidic phospholipid polar head groups ($K_a \sim 10^5$), and comparable to the affinity for the binding of Ca^{+2} to the Ca^{+2} ATPase protein ($K_a \sim 10^6$). Based on the localized nature and the position in the membrane profile of this lanthanide (III) ion high-affinity binding site centered at $z \sim 63$ Å and on previous reports of the ability of lanthanide (III) ions to act as Ca^{+2} analogues for the Ca^{+2} ATPase, we believe that this high-affinity binding site located in the "stalk" of the protein "headpiece" could also be a Ca^{+2} high-affinity binding site involved in the active transport of Ca^{+2} across the SR membrane.

Received for publication 26 March 1990 and in final form 24 September 1990.

REFERENCES

1. Inesi, G. 1985. Mechanism of calcium transport. *Annu. Rev. Physiol.* 47:573–601.
2. deMeis, L., and A. L. Viana. 1979. Energy interconversion by the Ca^{+2}-dependent ATPase of the sarcoplasmic reticulum. *Annu. Rev. Biochem.* 48:275–292.
3. Ikemoto, N. 1975. Transport and inhibitory Ca^{+2}-binding sites on the ATPase enzyme isolated from the sarcoplasmic reticulum. *J. Biol. Chem.* 250:7219–7224.
4. Leningher, A. L. 1982. Principles of Biochemistry. Worth Publishers, New York. 1011 pp.
5. Dupont, Y. 1980. Occlusion of divalent cations in the phosphorylated calcium pump of sarcoplasmic reticulum. *Eur. J. Biochem.* 109:231–238.
6. MacLennan, D., C. Brandl, B. Korczak, and M. Green. 1985. Amino-acid sequence of a Ca^{+2} + Mg^{+2}-dependent ATPase from rabbit muscle sarcoplasmic reticulum, deduced from its complementary DNA sequence. *Nature (Lond.).* 316:696–700.
7. Brandl, C., M. Green, B. Korczak, and D. MacLennan. 1986. Two Ca^{+2}-ATPase genes: homologies and mechanistic implications of deduced aminoacid sequence. *Cell.* 44:597–607.
8. Herbette, L., P. DeFoor, S. Fleischer, D. Pascolini, A. Scarpa, and J. K. Blasie. 1985. The separate profile structures of the functional calcium pump protein and the phospholipid bilayer within isolated sarcoplasmic reticulum membranes determined by x-ray and neutron diffraction. *Biochim. Biophys. Acta.* 817:103–122.
9. Clarke, D., K. Maruyama, T. Loo, E. Leberer, G. Inesi, and D. MacLennan. 1989. Functional consequences of glutamate, aspartate, glutamine, and asparagine mutations in the stalk sector of the Ca^{+2} ATPase of sarcoplasmic reticulum. *J. Biol. Chem.* 264:11246–11251.
10. Clarke, D., T. Loo, G. Inesi, and D. MacLennan. 1989. Location of high affinity Ca^{+2}-binding sites within the predicted transmembrane domain of the sarcoplasmic reticulum Ca^{+2} ATPase. *Nature (Lond.).* 339:476–478.
11. Stamatoff, J., P. Eisenberger, J. K. Blasie, J. Pachence, A. Tavormina, M. Erecinska, P. L. Dutton, and G. Brown. 1982. The location of redox centers in biological membranes determined by resonance x-ray diffraction. I. Observation of the resonance effect. *Biochim. Biophys. Acta.* 679:177–187.
12. Fairclough, R., R. Miake-Lye, R. Stroud, K. Hodgson, and S. Doniach. 1986. Location of terbium binding sites on acetylcholine receptor-enriched membranes. *J. Mol. Biol.* 189:673–680.
13. Blasie, J. K., and J. Stamatoff. 1981. Resonance x-ray scattering: its use in determining spatial relationships among metal atoms within macromolecules in a non-crystalline state. *Annu. Rev. Biophys. Bioeng.* 10:451–458.
14. Ladd, M. F., and R. A. Palmer. 1985. Structure Determinati oy X-Ray Crystalography. 2nd ed. Plenum Publishing Corp., New York. 502 pp.
15. Horrocks, W., and D. Sudnick. 1979. Lanthanide ion probes of structure in biology. Laser-induced luminescence decay constants provide a direct measure of the number of metal-coordinated water molecules. *J. Am. Chem. Soc.* 101:334–340.
16. Highsmith, S., and M. Head. 1983. Tb^{+3} binding to Ca^{+2} and Mg^{+2} binding sites on sarcoplasmic reticulum ATPase. *J. Biol. Chem.* 258:6858–6862.
17. Scott, T. 1983. Luminescence studies of Tb^{+3} bound to the high-affinity sites of the Ca^{+2}-ATPase of sarcoplasmic reticulum. *J. Biol. Chem.* 259:4035–4037.
18. Stephens, E., and C. Grisham. 1979. Lithium-7 nuclear magnetic resonance, water proton nuclear magnetic resonance, and gadolinium electron paramagnetic resonance studies of the sarcoplasmic reticulum calcium ion transport adenosine triphosphatase. *Biochemistry.* 18:4876–4885.
19. Bigelow, T., F. Squier, F. Fernandez-Belda, and G. Inesi. 1990. Interactions of calcium and lanthanides with the sarcoplasmic reticulum ATPase. *Biophys. J.* 57:279*a* (Abstr.).
20. MacLennan, D. 1970. Purification and properties of an adenosine triphosphatase from sarcoplasmic reticulum. *J. Biol. Chem.* 245:4508–4518.
21. MacFarland, B., and G. Inesi. 1971. Solubilization of sarcoplasmic reticulum with Triton X-100. *Arch. Biochem. Biophys.* 145:456–464.
22. Meisner, G., G. Conner, and S. Fleischer. 1973. Isolation of sarcoplasmic reticulum by zonal centrifugation and purification of Ca^{+2} pump and Ca^{+2} binding proteins. *Biochim. Biophys. Acta.* 298:246–269.
23. Lowry, O., N. Rosenbrough, A. Farr, and R. J. Randall. 1951. Protein measurement with folin reagent. *J. Biol. Chem.* 193:263–275.
24. Herbette, L., J. Marquardt, and J. K. Blasie. 1977. A direct

analysis of lamellar x-ray diffraction from hydrated oriented multilayers of fully functional sarcoplasmic reticulum. *Biophys. J.* 20:245–272.

25. Blasie, J. K., L. Herbette, and J. Pachence. 1985. Biological membrane structure as "seen" by x-ray and neutron diffraction. *J. Membr. Biol.* 86:1–7.
26. Asturias, F. J., D. Pascolini, and J. K. Blasie. 1990. Evidence that lipid lateral phase separation induces functionally significant structural changes in the Ca^{+2}-ATPase of the sarcoplasmic reticulum. *Biophys. J.* 58:205–217.
27. James, R. W. 1948. The optical principles of the diffraction of x-rays. *In* The Crystalline State. Vol. 2. L. Bragg, editor. Cornell University Press. Ithaca, NY. 135–192.
28. Herbette, L., A. Scarpa, J. K. Blasie, C. Wang, A. Saito, and S. Fleischer. 1981. Comparison of the profile structures of isolated and reconstituted sarcoplasmic reticulum membranes. *Biophys. J.* 36:47–72.
29. Schwartz, S., J. Cain, E. Dratz, and J. K. Blasie. 1975. An analysis of lamellar x-ray diffraction from disordered membrane multilayers with application to data from retinal rod outer segments. *Biophys. J.* 15:1201–1233.
30. Stroud, R. M., and D. A. Agard. 1979. Structure determination of asymmetric membrane profiles using an iterative Fourier method. *Biophys. J.* 25:495–512.
31. Pachence, J., P. L. Dutton, and J. K. Blasie. 1979. Structural studies of reconstituted reaction center/lecithin membranes. *Biochim. Biophys. Acta.* 548:348–373.
32. Pascolini, D., and J. K. Blasie. 1988. Moderate resolution profile structure of the sarcoplasmic reticulum membrane under "low" temperature conditions for the transient trapping of $E_1 \sim P$. *Biophys. J.* 54:669–678.
33. Asturias, F. J., and J. K. Blasie. 1989. Effect of Mg^{+2} concentration on Ca^{+2} uptake kinetics and structure of the sarcoplasmic reticulum membrane. *Biophys. J.* 55:739–753.
34. Hauser, H., C. Hickley, J. Krebs, B. A. Levine, M. Phillips, and R. J. Williams. 1977. *Biochim. Biophys. Acta.* 468:364–377.
35. Petersheim, M., H. N. Halladay, and J. Blodnieks. 1989. Tb^{+3} and Ca^{+2} binding to phosphatidylcholine: a study comparing data from optical, NMR, and infrared spectroscopies. *Biophys. J.* 56:551–557.
36. Bick, R., W. B. van Winkle, C. Tate, M. Entman, J. K. Blasie, and L. Herbette. 1987. Phospholipid fatty acyl chain asymetry in the membrane bilayer of isolated skeletal muscle sarcoplasmic reticulum. *Biochemistry.* 26:4831–4836.
37. Squier, T., D. Bigelow, F. J. Fernandez-Belda, L. deMeis, and G. Inesi. 1990. Calcium and lanthanide binding in the sarcoplasmic reticulum ATPase. *J. Biol. Chem.* 265:13713–13720.